the nature-made motors can power the transport system at the nano-scale. Although recent nanofabrication techniques have enabled the production of devices with dimension less than 10 nm, such nano-scale motors are not still available. Secondly, kinesin motor has high-energy conversion efficiency to 50% [6]. Finally, one can easily observe MTs gliding on kinesins by constructing an *in vitro* system.

As the basic geometry of the nano-scale transport systems, the kinesin-MT systems have been employed in a so-called inverted gliding assay in which MTs are propelled by surface-bound kinesins and act as carriers that transport attached cargos [7]. MTs used in the gliding assay system are usually grown from tubulin *in vitro* and have a length ranging from less than one micrometer to over tens of micrometers. It has been reported that a short MT captured by a single kinesin can rotate due to thermal diffusion depending on its size [8]. For a long MT, it is speculated that the leading tip can still fluctuate due to thermal diffusion as illustrated in Fig. 1, leaving the remaining part of the MT fixed on the kinesins due to crossbridges formed between the MT and the kinesins. This may potentially still lead to a change in the gliding direction of the MT. Since, in fact, MTs glide over a kinesin-coated surface in random directions, many studies have been attempted to control the gliding direction of MTs with chemical patterning of motor proteins [9], fabricated topographical patterns [5, 10], or their combination [11, 12, 13]. However, little is known of how the gliding direction of MTs can change with respect to their length, kinesin density and so on.

It has been reported by Böhm *et al.* [14] that the gliding velocity increases with decreasing kinesin density bound to glass surfaces, indicating the dependence of the number of kinesins per the unit length of MTs on the gliding velocity. Interestingly, they suggested that a high number of kinesins bound to the same MT may interfere each other with the gliding motion due to binding of kinesins to numerous tubulin dimers, possibly resulted in an inefficient generation of motility. It is of great interest here to study the effect of the length of MTs on the gliding velocity because conventionally available MTs have a wide range of length as noted above and also because this, of course, may be related to a high efficient motility assay. It is thus hypothesized that if the gliding velocity solely depends on the number of kinesins per the unit length of MTs, the gliding velocity will not change with the length.

Although fundamental motility properties of MTs are prerequisite for the development of reliable and high efficient nano-scale transport systems, only a few studies have been reported on characterization. Here, we characterize the motility properties of MTs gliding on kinesins by using an *in vitro* motility assay system. Characteristic parameters such as angular velocity and gliding velocity were determined, particularly focusing on the length of MTs and kinesin density, i.e. the spacing between neighboring kinesins.

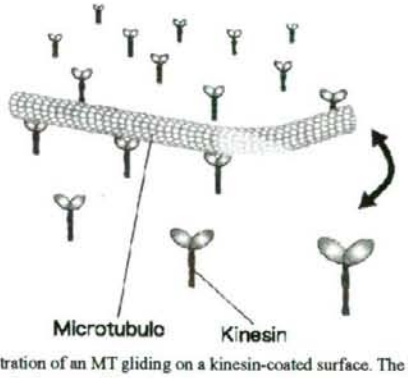

Fig. 1 Schematic illustration of an MT gliding on a kinesin-coated surface. The leading tip of the MT fluctuates in plane parallel to the surface, which is due to thermal diffusion.

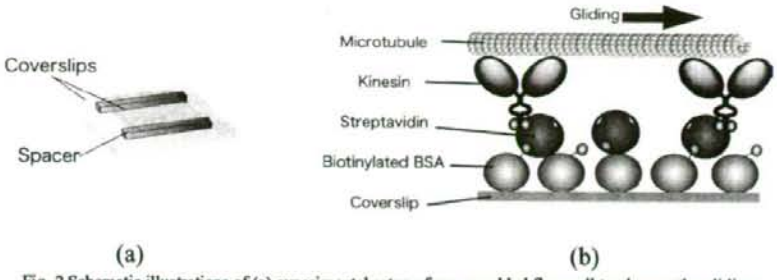

Fig. 2 Schematic illustrations of (a) experimental setup of an assembled flow cell to observe the gliding MTs and (b) an MT gliding on biotinylated kinesins immobilized on the surface via streptavidin and biotinylated BSA in the flow cell.

2. Materials and Methods

2.1 Protein preparation

MTs were prepared from bovine tubulin (TL238, Cytoskeleton, Denver, CO, USA) containing 20% rhodamine-labeled tubulin (TL331 M, Cytoskeleton, Denver, CO, USA). The tubulin was polymerized into MTs by incubating with 1 mM guanosine-5'-triphosphate (GTP) in BRB80 buffer (80 mM PIPES, 1 mM EGTA, 4 mM $MgSO_4$, pH 6.9) at 37°C for 1 h. Then the rhodamine-labeled MTs were diluted two-fold with BRB80 buffer containing 100 μM paclitaxel.

Kinesin was kindly provided by Prof. H. Higuchi (University of Tokyo, Japan). The kinesin gene (pGEX-DK411-BCCP) included the coding sequences for the 411 N-terminal residues of *Drosophila* kinesin heavy chain (DK-411) that has motor domain of kinesin required for movement [15], and biotin carboxyl carrier protein (BCCP) at the C-terminal [16].

2.2 Motility assay

Motility assay was performed as previously described [17] with some modifications. To observe the gliding MTs *in vitro*, a flow cell was fabricated as shown in Fig. 2(a). The flow cell was assembled by sandwiching 22 μm-thick spacers with two different sizes of glass coverslips (18 × 18 mm^2 and 26 × 36 mm^2, No. 1, Matsunami, Japan). BRB80 was used as the buffer for all experiments. Protein configuration including MTs and kinesins in association with streptavidin and biotinamidocaproyl-labeled bovine serum albumin (biotinylated BSA) in the flow cell is shown in Fig. 2(b). The flow cell was filled with 1 mg/ml biotinylated BSA for 2 min. After flushing with the BRB80 buffer at least twice, the flow cell was filled with 1 mg/ml streptavidin solution for 2 min. The flow cell was flushed twice again and was then filled with 38 μg/ml of kinesin solution for 2 min. Other two different concentrations of kinesin solution, 75 μg/ml (high density) and 7.5 μg/ml (low density) were also used in order to assess the effect of the spacing between kinesins on the MTs motility. The flow cell was finally filled with 1 mM adenosine-5'- [(β, γ)-imido] triphosphate, triethylammonium (AMP-PNP) solution containing MTs, followed by replacement with 1 mM adenosine triphosphate (ATP) solution containing oxygen scavenger additives (1.5% β-mercaptoethanol, 1.5 mg/ml bovine serum albumin, 15 μM paclitaxel, 30 mM glucose, 120 μg/ml glucose oxidase, 30 μg/ml catalase) and 0.1% methylcellulose. The experiments were performed at room temperature of 20°C controlled by air conditioning. The change in the temperature of the solution monitored with a thermometer during experiments was ± 0.4°C. Although it has been demonstrated that temperature affects the gliding velocity [18], this range of temperature difference can be assumed negligible. Time-lapse images of the gliding MTs in the flow cell were captured using an inverted fluorescent microscope (IX-71, Olympus, Tokyo, Japan) equipped with a CCD camera (Cascade 512B, Nippon Roper, Tokyo, Japan) and transferred to a PC for the

following image analysis.

2.3 Characteristic parameters

Image analysis was performed with image analysis software (Image J, National Institutes of Health, Bethesda, MD, USA). Characteristic parameters such as angular velocity and gliding velocity of MTs were determined with respect to the length of MTs (L) as follows. Firstly, the gliding velocity (V) was calculated from displacement of the leading tips of MTs every 5 s. The angular velocity (ω) was then determined as the rate of change in the orientation angle of the gliding velocity vector. Both the parameters were averaged over the period of observation and expressed as a mean. MTs shorter than 20 μm were analyzed because MTs longer than 20 μm in length was rarely constructed in this study. The spacing between neighboring kinesins was assessed roughly by following the trajectories of the MTs. Figure 3 shows the images of MTs to estimate the spacing between kinesins. We observed some MTs transiently showing partial winding track (Fig. 3(b)). By superimposing the time-lapse images of those MTs, the points that the MTs always passed through were assumed to reflect the kinesin positions, and the distance between the points was measured (arrows in Fig. 3(c)).

2.4 Statistical analysis

Because of an unequal variance in several variables, mean angular velocities and mean gliding velocities between kinesin densities were compared by the Steel-Dwass test. The association between MT length and mean angular velocity or mean gliding velocity was assessed by the Pearson's correlation coefficient. All hypothesis tests were performed using a significance level of 0.05. Data were shown as mean ± standard deviation (SD).

3. Results

3.1 Angular velocity

Typical time-lapse images of the gliding MTs under 38 μg/ml of kinesin solution are shown in Figs. 4(a) and (b) for a long MT with 8.0 μm long and a short MT with 2.9 μm long, respectively. The images clearly showed that the long MT glided over the surface along a rather straight path, whereas the short MT created a random path. Figures 4(c) to (g) show the trajectories of the gliding MTs in different ranges of the length. The trajectories are summarized by the length at 2 μm intervals up to 10 μm in order to prevent confusing their tendency and are plotted every 5 s up to 120 s. The trajectories of MTs shorter than 4 μm showed that the movement is random over the period of time (Figs. 4(c) and (d)). In contrast, the trajectories of MTs longer than 6 μm showed more straight and smooth movement (Figs. 4(f) and (g)).

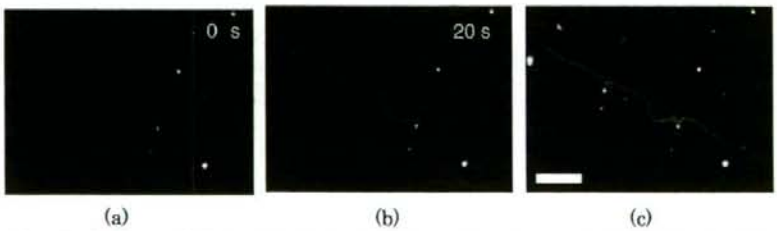

(a) (b) (c)

Fig. 3 Typical images of gliding MTs for estimation of the spacing between kinesins. (a and b) Sequential images of a gliding MT. The MT traveling in a straight track (a) suddenly showed winding shapes (b). (c) The points MTs always passed through on superimposed time-lapse images for 0–20 s (filled circles) gave the position of kinesin, and the spacings between kinesins were measured as the distance between points (arrows). Bar = 5 μm.

The measured kinesin spacings were 7.8 ± 2.7 (n = 29), 4.7 ± 1.3 (n = 43), and 3.1 ± 0.9 (n = 46) μm for 7.5, 38, and 75 μg/ml of kinesin densities, respectively. Figures 5(a) to (c) shows the length-dependency in the angular velocity at the three different kinesin densities. Under all the kinesin densities, the angular velocity substantially tended to decrease as the length of MTs increased, and finally achieved the plateau level. We separately analyzed the correlation between the angular velocity and the MT length by dividing the MTs into two groups: MTs shorter or longer than kinesin spacings. For the MTs shorter than the spacing between kinesins, the correlation coefficients of the linear regression lines were significant under all kinesin densities (r = -0.63, p < 0.001 (7.5 μg/ml); r = -0.50, p < 0.01 (38 μg/ml); r = -0.68, p < 0.05 (75 μg/ml)). On the other hand, the correlation coefficients of the regression lines were not significant for the MTs longer than kinesin spacings (r = -0.01, p = 0.958 (7.5 μg/ml); r = -0.01, p = 0.750 (38 μg/ml); r = 0.03, p = 0.854 (75 μg/ml)), indicating that the angular velocity of MTs longer than the kinesin spacing seemed to be independent of their length. The mean angular velocity of gliding MTs longer than the kinesin spacings was significantly higher at low kinesin density (3.1 ± 1.3, n = 23 (7.5 μg/ml)) than at the middle (1.9 ± 0.9, n = 38, p < 0.001 (38 μg/ml)) and high kinesin densities (1.8 ± 0.7, n = 44, p < 0.001 (7.5 μg/ml)) (Fig. 5(d)).

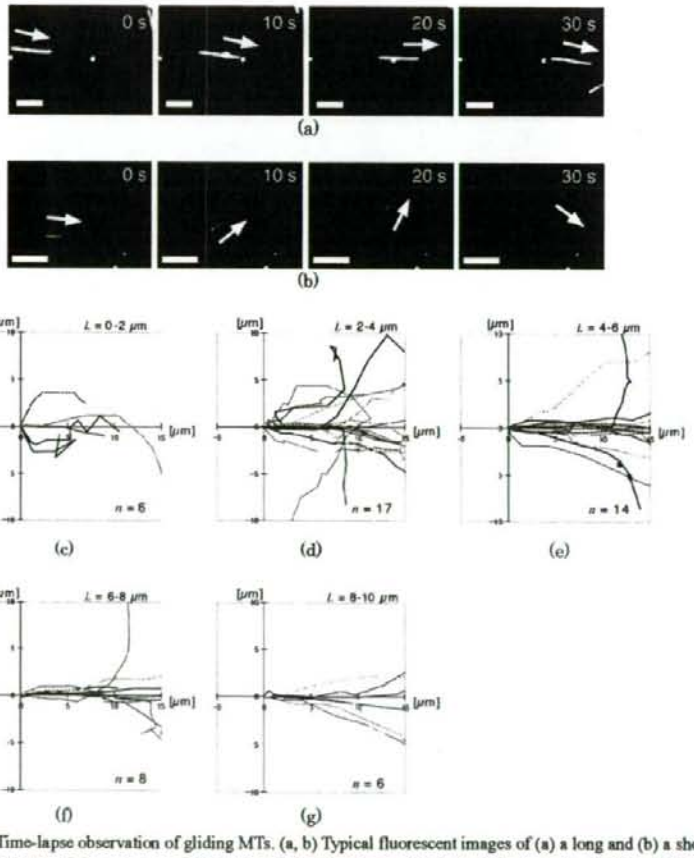

Fig. 4 Time-lapse observation of gliding MTs. (a, b) Typical fluorescent images of (a) a long and (b) a short gliding MT. Bar = 5 μm. Arrows indicate the gliding directions of MTs. (c–f) Trajectories of gliding MTs for (c) L = 0–2, (d) 2–4, (e) 4–6, (f) 6–8, and (g) 8–10 μm. The gliding direction at the initial time is expressed from left to right.

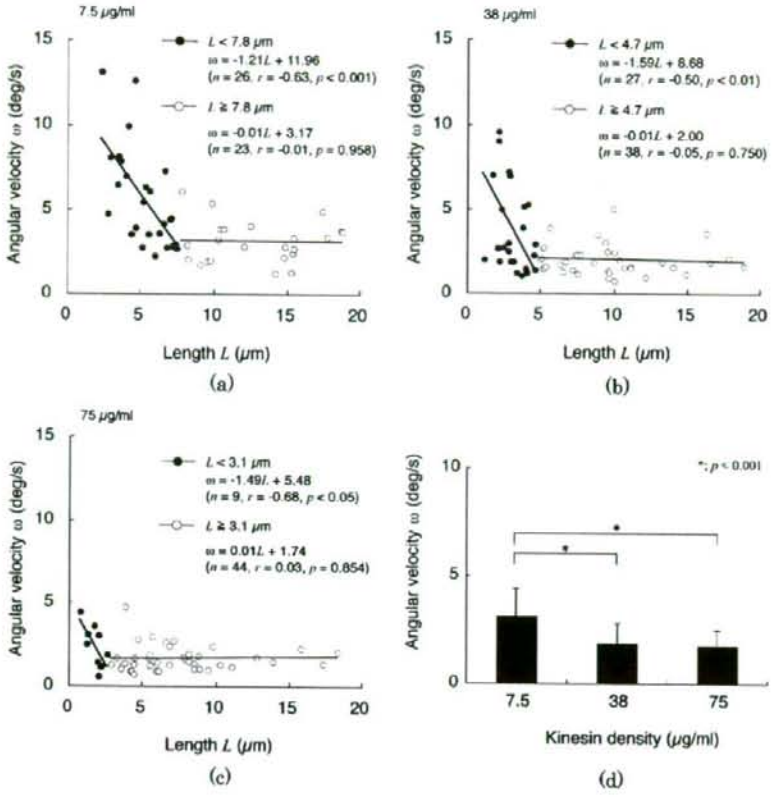

Fig. 5 The angular velocity of gliding MTs. (a–c) The angular velocity plotted against MT length for kinesin densities of (a) 7.5, (b) 38, and (c) 75 μg/ml. The filled and open circles show the data for MTs shorter and longer than the estimated kinesin spacing, respectively. The solid lines were obtained by least squares regression. (d) The averaged angular velocity for the MTs longer than the estimated kinesin spacings.

3.2 Gliding velocity

Figures 6(a) to (c) shows the length-dependency in the gliding velocity at the three different kinesin densities. For all the kinesin densities, the correlation coefficients between the gliding velocity and the MT length were not significant ($r = 0.28$, $p = 0.054$ (7.5 μg/ml); $r = 0.19$, $p = 0.13$ (38 μg/ml); $r = 0.24$, $p = 0.079$ (75 μg/ml)). The gliding velocities for all the length were 0.45 ± 0.15, 0.32 ± 0.10, and 0.35 ± 0.10 μm/s for 7.5, 38, and 75 μg/ml kinesin densities, respectively (Fig. 5(d)). The gliding velocity at the low kinesin density was significantly higher than those at the middle ($p < 0.001$) and high kinesin densities ($p < 0.001$). The independency of MT length on the gliding velocity was also observed for either case of the analysis for only MTs shorter or longer than kinesin spacings (data not shown).

4. Discussion

For developing high throughput nano-scale transport systems, fundamental motility properties of carriers such as directionality and velocity should be well controlled. As shown in Fig. 5, the angular velocity significantly decreased with increasing the length of MTs for the MTs shorter than the estimated kinesin spacings. This result can be explained by the larger thermal fluctuation for longer MTs captured by a single kinesin [8]. On the

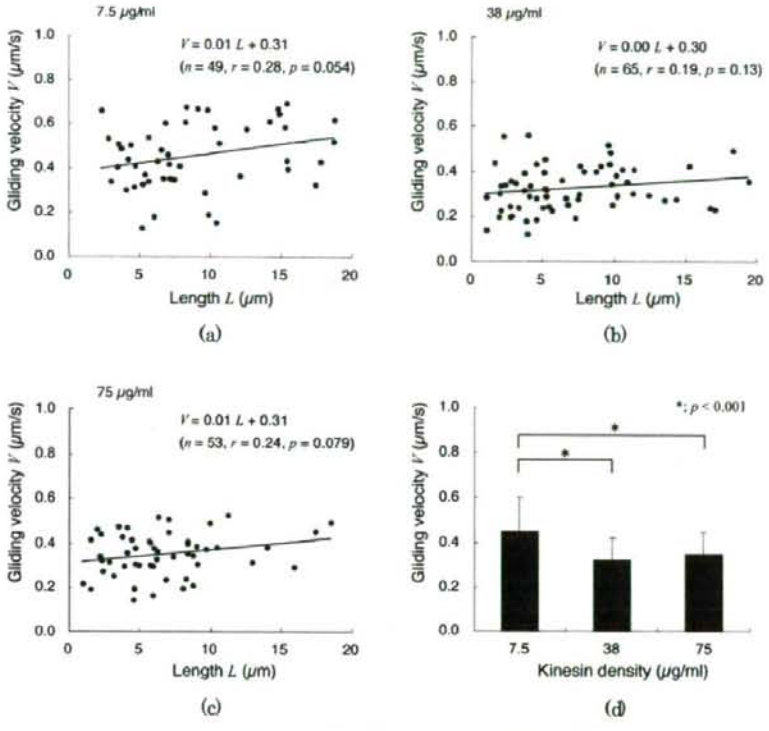

Fig. 6 The gliding velocity of MTs. (a–c) The gliding velocity plotted against their length for kinesin densities of (a) 7.5 μg/ml, (b) 38 μg/ml and (c) 75 μg/ml. The solid lines were obtained by least squares regression. (d) The averaged gliding velocity with regard to the kinesin densities.

other hand, the angular velocity for MTs longer than the spacing between kinesins was independent of the MT length. This is probably due to the fact that, within that range of the MT length, not a single kinesin but multiple kinesins could form crossbridges with the MTs and the crossbridges could work as fixed points against which reaction moments can be generated by the externally-driven thermal fluctuations. Although it is also possible that more crossbridges could decrease the deflection angle of the MT leading tip due to thermal fluctuations given by the strength of materials theory, the result obtained in this study shows that the effect was negligible small. In addition, as shown in Fig. 5(d), the angular velocity substantially increased as the kinesin density decreased, in other words, as the spacing between kinesins increased. These results strongly indicate that the number of associated kinesins with MTs would be a critical factor in the gliding direction of MTs. It is thus possible that longer MTs associated with multiple kinesins at higher kinesin density may have higher directionality of the gliding MTs.

It is important to note that detaching of MTs from the kinesin surfaces was frequently observed, with the rate depending on the length of MTs. The maximum lengths that the detaching was observed were 7.9, 4.1, and 2.3 μm for 7.5, 38, and 75 μg/ml kinesin densities, respectively. These values of the lengths were closely related to the estimated spacing between kinesins. Gliding MTs shorter than the kinesin spacing are likely to fail to catch next kinesin to glide ahead. It is also important to address the possible gliding distance. Since it is difficult to observe the gliding MTs until detaching due to the limited observation area, the gliding distance cannot be directly measured. In a separate experiment, it was confirmed that MTs were found to still glide even after 1 h. If the gliding velocity is,

for example, assumed to be 0.3 μm/s from Fig. 5, the gliding distance can be estimated more than 1 mm at 1 h. Stracke *et al.* [19] have also observed MTs gliding longer than 1 mm. Both preventing the detaching of MTs and the MTs gliding for a long distance would be also important for the transport system.

The gliding velocity of MTs obtained in this study had no significant correlation with the length of MTs for all the kinesin densities. Although Hunt *et al.* [20] have showed that the MT length did not affect their gliding velocity, the mechanism is still unclear. A single kinesin can produce the force of ~ 6 pN at maximum in a single step [21], presumably indicating that an increase in the number of kinesins interacting with MTs may result in an increase in the driving forces. Therefore, it is supposed that the driving forces by kinesins and drag forces acting on the gliding MTs due to the solution viscosity should be in equilibrium. However, the drag forces was, for example, estimated to be 0.05 and 0.1 pN for the MT length of 5 μm and 10 μm, respectively, which are much lower than the driving forces. Böhm *et al.* [14] have reported that the gliding velocity showed a logarithmic decrease with increasing kinesin density bound to glass surfaces, indicating the dependence of the number of kinesins per the unit length of MTs on the gliding velocity. They have also suggested that binding of a high number of kinesin molecules to the same MT may hinder movement of each kinesin, resulting in an inefficient generation of motility. Although this mechanism is still unknown, we also showed that the gliding velocity of MTs was not affected by the change of the MT length. These results indicate that the gliding velocity of MTs is potentially affected not by the MT length but by the number of kinesins per the unit length of MTs. Therefore, it is important to consider the effect of the MT length and kinesin density simultaneously.

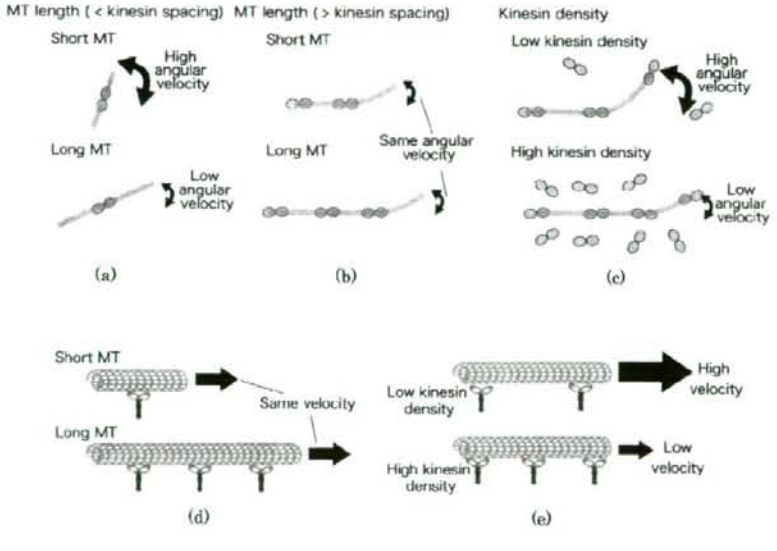

Fig. 7 A possible underlying mechanism to explain the motility properties of MTs with respect to the their length and kinesin density. (a) Dependence of the MT length for MTs shorter than kinesin spacings and (b) independence of the MT length for MTs longer than kinesin spacings. (c) Dependence of kinesin density on the angular velocity of MTs. (d) Independence of the MT length and (e) dependence of kinesin density on the gliding velocity of MTs.

Taken all the results together, we propose a concept to explain the possible mechanism for the angular velocity and the gliding velocity, as illustrated in Fig. 7. In Fig. 7(a), an MT shorter than the critical spacing between kinesins is supposed to be captured by a single kinesin and can rotate due to thermal diffusion depending on its length and shows high angular velocity. For an MT longer than the spacing captured by more than two kinesins, the angular velocity remains low and constant value (Fig. 7(b)). In Fig. 7(c), angular velocity is lower for higher kinesin density, probably because the increase of kinesin density results in an increase of the number of kinesins that MTs can be in contact with before showing large deflection. As shown in Fig. 7(d), the gliding velocity is independent on the MT length, whereas, Fig. 7(e) shows the gliding velocity depends on kinesin density; that is, increase in velocity with decreasing the kinesin density.

In summary, we characterized the motility properties of MTs gliding on kinesin-coated surface with respect to their length and kinesin density. The angular velocity of the gliding MTs significantly decreased with increasing their length for MTs shorter than kinesin spacings and achieved a plateau for MTs longer than kinesin spacings. Moreover, the angular velocity was substantially higher at lower kinesin density. These results suggest that both the number of associated kinesins with MTs and the kinesin spacing may contribute to the gliding direction. In contrast, the gliding velocity of the gliding MTs was not significantly affected by their length and was significantly increased at the low kinesin density compared to the other two densities, indicating the dependence of the gliding velocity on the number of kinesins per the unit length of MTs. These results reveal that long MTs associated with many kinesins would have high directionality, and that low kinesin densities would produce the MTs gliding of high velocity, towards development of high throughput nano-scale transport systems.

Acknowledgements

The authors thank Prof. Hideo Higuchi for technical support for preparation of proteins and acknowledge the support of Tohoku University Global COE Program "Global Nano-Biomedical Engineering Education and Research Network Center".

References

(1) Kerssemakers, J., Howard, J., Hess, H., and Diez, S., The distance that kinesin-1 holds its cargo from the microtubule surface measured by fluorescence interference contrast microscopy, *Proceedings of the National Academy of the Sciences of the United States of America*, Vol. 103, No. 43 (2006), pp. 15812-15817.

(2) Sheetz, M.P., Vale, R., Schnapp, B., Schroer, T., and Reese, T., Vesicle movements and microtubule-based motors, *Journal of Cell Science*, Vol. 5 (1986), pp. 181-188.

(3) Schroer, T.A., Schnapp, B.J., Reese, T.S., and Sheetz, M.P., The role of kinesin and other soluble factors in organelle movement along microtubules, *Journal of Cell Biology*, Vol. 107, No. 5 (1988), pp.1785-1792.

(4) Brunner, C., Wahnes, C., and Vogel, V., Cargo pick-up from engineered loading stations by kinesin driven molecular shuttles, *Lab on a Chip*, Vol. 10 (2007), pp. 1263-1271.

(5) Hess, H., Clemmens, J., Qin, D., Howard, J., and Vogel, V., Light-controlled molecular shuttles made from motor proteins carrying cargo on engineered surfaces, *Nano Letters*, Vol. 1, No. 5 (2001), pp. 235-239.

(6) Howard, J., *Mechanics of Motor Proteins and the Cytoskeleton*, (2001), p. 254, Sinauer Associates, Inc.

(7) Howard, J., Hudspeth, A.J., and Vale, R.D., Movement of microtubules by single kinesin molecules, *Nature*, Vol. 342, No. 9 (1989), pp. 154-158.

(8) Hunt, A.J. and Howard, J., Kinesin swivels to permit microtubule movement in any direction, *Proceedings of the National Academy of the Sciences of the United States of*

America, Vol. 90, No. 24 (1993), pp. 11653-11657.

(9) Suzuki, H., Yamada, A., Oiwa, K., Nakayama, H, and Mashiko, S., Control of actin moving trajectory by patterned poly (methylmethacrylate) tracks, *Biophysical Journal*, Vol. 72, No. 5 (1997), pp. 1997-2001.

(10) Riveline, D., Ott, A., Julicher, F., Winkelmann, D.A., Cardoso, O., Lacapère, J.J., Magnúsdóttir, S., Viovy, J.L., Gorre-Talini, L., and Prost, J., Acting on actin: the electric motility assay, *European Biophysics Journal*, Vol. 27, No. 4 (1998), pp. 403-408.

(11) Hiratsuka, Y., Tada, T., Oiwa, K., Kanayama, T., and Uyeda, T.Q., Controlling the direction of kinesin-driven microtubule movements along microlithographic tracks, *Biophysical Journal*, Vol. 81, No.3 (2001), pp. 1555-1561.

(12) Moorjani, S.G., Jia, L., Jackson, T.N., and Hancock, W.O., Lithographically patterned channels spatially segregate kinesin motor activity and effectively guide microtubule movements, *Nano Letters*, Vol. 3, No. 5 (2003), pp. 633-637.

(13) Hess, H., Matzke, C.M., Doot, R.K., Clemmens, J., Bachand, G.D., Bunker, B.C., and Vogel, V., Molecular shuttles operating undercover: A new photolithographic approach for the fabrication of structured surfaces supporting directed motility, *Nano Letters*, Vol. 3, No. 12 (2003), pp. 1651-1655.

(14) Böhm, K.J., Stracke, R., and Unger, E., Speeding up kinesin-driven microtubule gliding *in vitro* by variation of cofactor composition and physicochemical parameters, *Cell Biology International*, Vol. 24, No. 6 (2000), pp. 335-341.

(15) Inoue, Y., Toyoshima, Y.Y., Iwane, A.H., Morimoto, S., Higuchi, H., and Yanagida, T., Movements of truncated kinesin fragments with a short or an artificial flexible neck, *Proceedings of the National Academy of the Sciences of the United States of America*, Vol. 94, No. 14 (1997), pp. 7275-7280.

(16) Kamei, T., Kakuta, S., and Higuchi, H., Biased binding of single molecules and continuous movement of multiple molecules of truncated single-headed kinesin, *Biophysical Journal*, Vol. 88, No. 3 (2005), pp. 2068-2077.

(17) Howard, J., Hudspeth, A.J., and Vale, R.D., Movement of microtubules by single kinesin molecules, *Nature*, Vol. 342, No. 6246 (1989), pp. 154-148.

(18) Böhm, K.J., Stracke, R., Baum, M., Zieren, M., and Unger, E., Effect of temperature on kinesin-driven microtubule gliding and kinesin ATPase activity, *FEBS Letters*, Vol. 466, No. 1 (2000), pp. 59-62.

(19) Stracke, R., Böhm, K.J., Burgold, J., Schacht, H-J., and Unger, E., Physical and technical parameters determining the functioning of a kinesin-based cell-free motor system, *Nanotechnology*, Vol. 11, No. 2 (2000), pp. 52-56.

(20) Hunt, A.J., Gittes, F., and Howard, J., The force exerted by a single kinesin molecule against a viscous load, *Biophysical Journal*, Vol. 67, No. 2 (1994), pp. 766-781.

(21) Svoboda, K. and Block, S.M., Force and velocity measured for single kinesin molecules, *Cell*, Vol. 77, No. 5 (1994), pp. 773-784.

Experimental Mechanics (2009) 49:125–134
DOI 10.1007/s11340-008-9143-3

Morphological Responses of Vascular Endothelial Cells Induced by Local Stretch Transmitted Through Intercellular Junctions

Y. Ueki · N. Sakamoto · T. Ohashi · M. Sato

Received: 6 June 2007 / Accepted: 24 March 2008 / Published online: 23 April 2008

Abstract It has been well established that mechanical stimuli including fluid shear stress and cyclic stretch play a key role in endothelial cell (EC) remodeling. However, in contrast to global remodeling to these mechanical stimuli, little is known of how local mechanical forces are transmitted through cells to induce cell remodeling leading to alteration in cell functions. In this study, we demonstrated that EC remodeling can be exerted by local tension generated in a neighboring EC. In this technique, a glass microneedle was used to apply local stretch in an EC in confluent monolayer and the resulting tension is transmitted to a neighboring EC across intercellular junctions. Local stretch induced reorientation and elongation of ECs parallel to the direction of stretch associated with reorganization of stress fibers. In addition, recruitment of Src homology 2-containing tyrosine phosphatase-2, binding to intercellular adhesion molecules platelet-endothelial cellular adhesion molecules-1, was selectively observed at the force-transmitted intercellular junctions after application of local stretch. These findings suggest that intercellular junctions can not only transmit but also sense local forces, and are potentially involved in EC mechanotransduction pathways.

Keywords Endothelial cell remodeling · Stress fibers · Mechanotransduction · Intercellular junction · Adhesion molecules

Y. Ueki (✉) · N. Sakamoto · T. Ohashi · M. Sato
Department of Bioengineering and Robotics,
Graduate School of Engineering, Tohoku University,
6-6-01 Aramaki-aoba,
Sendai 980-8579, Japan
e-mail: ueki@bml.mech.tohoku.ac.jp

N. Sakamoto
e-mail: naoya@bml.mech.tohoku.ac.jp

T. Ohashi
e-mail: ohashi@bml.mech.tohoku.ac.jp

M. Sato
Department of Biomedical Engineering,
Graduate School of Biomedical Engineering, Tohoku University,
6-6-01 Aramaki-aoba,
Sendai 980-8579, Japan
e-mail: sato@bml.mech.tohoku.ac.jp

Introduction

Endothelial cells (ECs) lining inner surfaces of blood vessels are exposed to a variety of mechanical stimuli including fluid shear stress due to blood flow, cyclic stretch due to the wall deformation, and hydrostatic pressure due to blood pressure. Since the relationship between EC morphology and mechanical conditions has been implicated in vascular pathology such as atherosclerosis, in vitro model systems have been widely used to investigate the effects of mechanical stimuli on EC remodeling. Most previous studies have exclusively applied global mechanical stimuli including fluid shear stress [1–4], cyclic stretch [5, 6] and hydrostatic pressure [7, 8] to cultured EC monolayer. For example, under exposure to fluid shear stress, ECs exhibit elongation and alignment parallel to the direction of flow concomitant with reorganization of actin stress fibers (SFs) [2, 4]. It is also well known that ECs exposed to cyclic stretch elongate and align perpendicular to the direction of stretch [5]. Furthermore, pressure-imposed ECs elongate with random orientation [7]. Thus, ECs respond very specifically to the type of mechanical stimuli, raising the question of how externally applied mechanical forces transmit in cells and where the transmitted forces are sensed and converted into biochemical signals. It has been suggested that mechanotransduction of ECs may occur at

specific sites located in cell membrane (e.g. stretch activated channels (SACs)), attachment points of ECs to extracellular matrix (e.g. integrins), intercellular junctions (e.g. platelet-endothelial cellular adhesion molecules-1, PECAM-1) and more likely a combination of these sites. However, the details of these mechanotransducers in cell signaling pathways remain unclear, because, in part, there is a possibility that these mechanotransducers can be simultaneously activated by the globally applied mechanical stimuli. Therefore, it is necessary to develop an experimental method, with which each mechanotransducer can be selectively stimulated.

Intercellular junctions of ECs involve adherens-junctions, tight-junctions, gap-junctions and PECAM-1 junctions. Particularly, adherens-junctions composed of VE-cadherin which is connected to actin-cytoskeleton via α/β catenins are thought to exclusively mediate forces at intercellular junctions by forming homophilic binding, probably because mechanical coupling by adherens-junctions may be stiffer than the other junctions. Recently, there has been a growing attention on the role of intercellular adhesion molecules with implications of EC mechanotransduction signalling pathways. PECAM-1 is known to form homophilic binding between neighboring ECs [9] in the vicinity of adherens-junctions and be connected to actin-cytoskeletons via β/γ catenins [10]. Previous reports revealed that ECs under sparse conditions do not show morphological changes in response to fluid shear stress [11, 12]. Osawa et al. [13] reported that PECAM-1 is rapidly tyrosine-phosphorylated when ECs are exposed to fluid shear stress or hyper osmotic shock, and bind to a protein tyrosine phosphatase Src homology 2-containing tyrosine phosphatase-2 (SHP-2) to activate intracellular signal cascades. Tzima et al. [14] reported that PECAM-1-mediated mechanotransduction is involved in the upstream of the integrin signaling cascade, leading to cytoskeletal reorganization in flow conditioned ECs. This leads to an idea that transmitted forces at adherens-junctions may stimulate PECAM-1 phosphorylation, leading to SHP-2 activation followed by morphological changes of ECs. Thus, PECAM-1 may be responsible for morphological responses to mechanical stimuli transmitted through intercellular junctions serving as one of principal mechanotransducers.

To test this hypothesis, in this study, local stretch was applied to an EC by using a microneedle to selectively stimulate intercellular junctions between the EC and a neighboring EC. After application of mechanical stimuli, morphological changes of the neighboring EC were fluorescently observed to test the hypothesis that local stimuli are transmitted via intercellular junctions and induce EC remodeling. In addition, localization of SHP-2 was observed to assess whether PECAM-1 is involved in the mechanotransduction pathways.

Materials and Methods

Cell Culture and Transfection

Human umbilical vein endothelial cells (HUVECs) were obtained from umbilical veins with trypsin treatment adapted from Sakamoto et al. [15]. Cells were cultured in Medium 199 (Invitrogen, USA) containing 20% fetal bovine serum (Sigma-Aldrich, USA), 10 ng/ml basic fibroblast growth factor (Austral Biologicals, USA) and penicillin-streptomycin (Invitrogen), and were used from the third to the sixth passage. For experiments, cells were plated on a glass base culture dish (ø=35 mm, Asahi Techno Glass, Japan) coated with 0.1% gelatin (Sigma-Aldrich). A plasmid encoding enhanced green fluorescent protein (EGFP)-actin (Clontech, USA) was transfected into HUVECs with a liposomal method using Lipofectin (Invitrogen) according to the manufacturer's protocol for visualization of actin cytoskeleton.

Local Stretch Experiment

Figure 1 shows the experimental setup used to apply local stretch. A glass microneedle with a diameter of ca. 1 μm

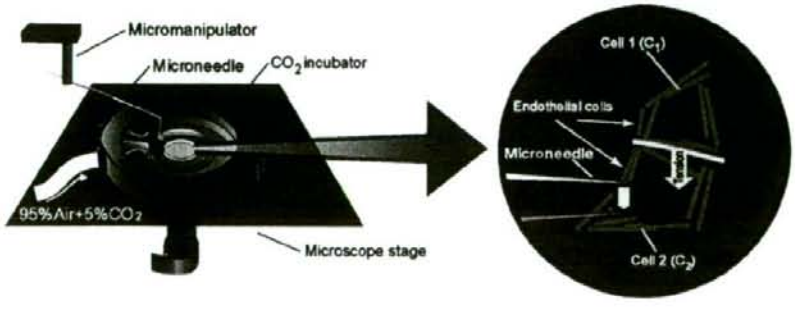

Fig. 1 Schematic illustrations of experimental system for local stretch application. A microneedle was used to apply local stretch to C_2, possibly inducing remodeling of C_1 via intercellular junctions. The experiments were performed in a CO_2 incubator at 37°C and 5% CO_2

was made from a glass tube (ø=1 mm, GD-1, Narishige, Japan) using a pipette puller (PP-83, Narishige, Japan) and manipulated by a 3-D hydraulic micromanipulator. A pair of ECs (cell 1 (C_1) and cell 2 (C_2)) in the figure) expressing EGFP-actin were selected under a confocal laser scanning microscope (CLSM, FV1000, Olympus, Japan), and the nucleus of C_2 was then moved horizontally by 10 μm by manipulating the glass microneedle to locally stretch C_1. This procedure allows us to mimic cell deformation induced by externally applied local tension via intercellular junctions between C_1 and C_2. In a separate study, particle tracer velocimetry (PTV) method was performed to calculate distribution of intracellular deformation induced by local stretch by using a software (Flowvec, Library, Japan) (Fig. 2). The result showed that high displacement was observed specifically at the intercellular junctions between C_1 and C_2, confirming force transmission across the junctions. After application of local stretch, fluorescent images were obtained up to 60 min at intervals of 5 min with the CLSM to assess features of C_1 remodeling process. All procedures were performed in a CO_2 incubator (MI-IBC, Olympus) mounted on the microscope stage to maintain the cell culture environment at 37°C and 5% CO_2.

Image Analysis

Image analysis was performed to evaluate morphological and cytoskeletal changes of C_1 using the following parameters: angle of cell orientation, cell aspect ratio, angle of SF orientation and uniformity index of SF. Angle of cell orientation and cell aspect ratio were calculated with the public domain program Image J version 1.37v (National Institute of Health, USA). A cell outline was manually extracted from a fluorescence image of GFP-actin by tracing the cell edge. An equivalent ellipse for the cell outline was automatically determined with a function of the software. An angle between the major axis of the ellipse and the direction of stretch was then defined as the angle of cell orientation. A ratio of length of the minor axis to the major axis was defined as the cell aspect ratio, with being 1.0 for circles and approaching zero for highly elongated shape. Analyses were performed on the fluorescent images obtained at every 5 min after application of local stretch. See Appendix for details of the angle of SF orientation and the uniformity index of SF.

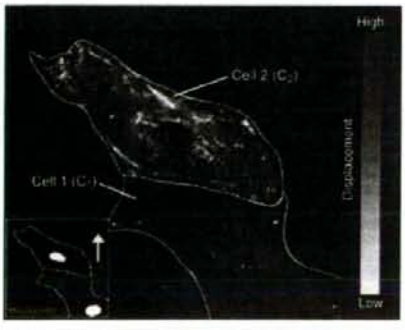

Fig. 2 Distribution of intracellular displacement calculated by using PTV method. Longer arrows represent higher displacement. Applied local stretch in C_2 was found to be transmitted to C_1 at intercellular junctions

SACs Blocking Experiment

In order to inhibit function of SACs, 20 μM $GdCl_3$ (Wako pure chemical, Japan) was added to cell culture medium at 30 min before application of local stretch.

Immunofluorescence

Localization of SHP-2 was examined with immunofluorescence. ECs were pre-incubated with 1 mM $NaVO_3$ (Wako Pure Chemical, Japan) for 30 min to enhance tyrosine phosphorylation before application of local stretch. Five minutes after the mechanical loading, ECs were then fixed in 4% paraformaldehyde (Wako Pure Chemical) containing 1 mM $NaVO_3$ for 15 min at 4°C. Next, ECs were permeabilized with 0.1% Triton X (Wako Pure Chemical), blocked with Block ace (Dainippon Sumitomo Pharma, Japan), and stained with anti-SHP-2 mouse monoclonal antibody (Santa Cruz Biotechnology, USA) and Alexa fluor 594 anti-mouse IgG (Invitrogen).

Statistical Analysis

Statistical comparisons in morphological parameters were performed using repeated measures analysis of variance (ANOVA) followed by Bonferroni's multiple comparison (0 min vs 30 min, 60 min). A p value less than 0.05 was considered as significant. Data are expressed a mean± SEM.

Results

Morphological Changes of ECs After Application of Local Stretch

Typical florescent images of EGFP-actin were shown in Fig. 3 at 0 min, 30 min and 60 min after application of local stretch. The observed cell C_1 initially elongated perpendicular to the direction of stretch [Fig. 3(a)] exhibited contraction at 30 min [Fig. 3(b)] followed by elongation

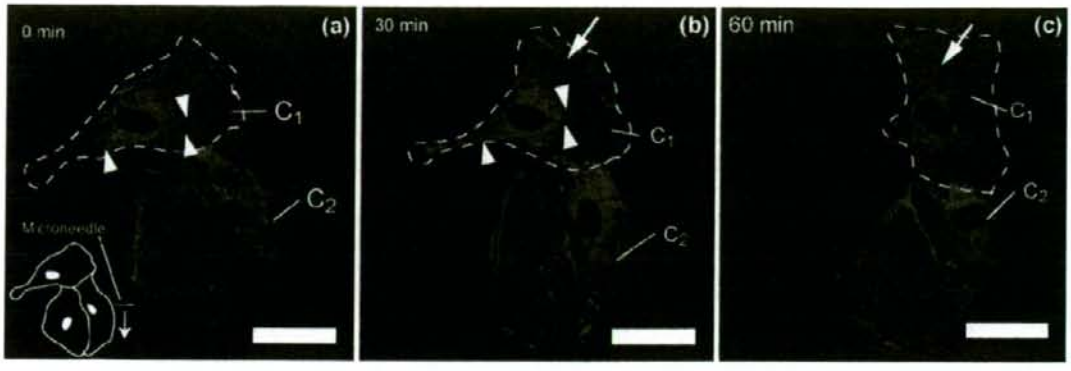

Fig. 3 Typical examples of fluorescent images of EGFP-actin at (**a**) 0 min, (**b**) 30 min, and (**c**) 60 min after application of local stretch. Broken lines indicate the edge of C_1. The horizontally elongated C_1 at 0 min (**a**) showed contraction at 30 min (**b**) and re-elongated parallel to the direction of the stretch at 60 min (**c**). Preexisting SFs at 0 min (**a**) disappeared at 30 min (**b**) and new SFs formation was observed at 60 min (**c**). Bar=40 μm

parallel to the direction of stretch at 60 min [Fig. 3(c)]. Concurrently with these morphological changes, SFs initially orientated perpendicular to the direction of stretch at 0 min [Fig. 3(a), arrowheads], and disappeared [Fig. 3(b), arrowheads] while formation of new SFs parallel to the direction of stretch was observed [Fig. 3(b), arrow] at 30 min. The new SF formation was continuously observed at 60 min [Fig. 3(c), arrow].

Figure 4 represents distribution of the angle of cell orientation and the cell aspect ratio of the observed cell C_1 at 0 min, 30 min and 60 min. From different types of initial cell morphology, the experimented data can be divided into two groups: Group A, ECs with angle of cell orientation >60° and aspect ratio <0.5; Group B, the rest of Group A. Roughly, distribution of the two groups is schematically drawn in the figure by ellipsoids. For both Groups, the angle of cell orientation significantly decreased from 0 min [Fig. 4(a), 71.3±4.4°, 53.3±4.6° for Groups A and B, respectively] to 60 min [Fig. 4(c), 52.1±6.8°, and 29.0±3.7° for Groups A and B respectively, $p<0.05$ vs 0 min for both groups]. For Group A, aspect ratio significantly increased from 0 min [Fig. 4(a), 0.42±0.02] to 30 min [Fig. 4(b), 0.57±0.07, $p<0.05$ vs 0 min] and then decreased at 60 min [Fig. 4(c), 0.53±0.08, NS vs 0 min]. On the other hand, for Group B, aspect ratio did not show a significant change from 0 min [Fig. 4(a), 0.57±0.05] to 30 min [Fig. 4(b), 0.55±0.07] and significantly decreased at 60 min [Fig. 4(c), 0.47±0.06, $p<0.05$ vs 0 min].

Time course of change in the SF parameters is summarized in Fig. 5. Angle of SF orientation for both groups significantly decreased at 60 min [Fig. 5(a), $p<0.05$, vs 0 min]. For Group A, change in the uniformity index was not significant between 0 min and 60 min [Fig. 5(b)] while the uniformity index significantly increased at 60 min for Group B [Fig. 5(b), $p<0.05$ vs 0 min].

SACs Blocking Experiment

SACs blocking experiment was performed on Group B with treatment of $GdCl_3$. Treated cells showed the similar time course of change in morphology, and morphological parameters showed no significant difference compared to those of non-treated control cells (data not shown). This result indicates that SACs should not be involved in the present remodeling.

Change in Distribution of SHP-2 After Application of Local Stretch

Figure 6 represents typical fluorescent images of EGFP-actin and anti-SHP-2 for control [Fig. 6(a,b,c)] and $GdCl_3$-treated ECs [Fig. 6(d,e,f)] after application of local stretch. For control ECs, recruitment of SHP-2 was clearly observed at the intercellular junctions between C_1 and C_2 [Fig. 6(b,c)]. For $GdCl_3$ -treated ECs, localization of SHP-2 was still observed at the intercellular junctions, suggesting that applied mechanical loading can be transduced into molecular signals [Fig. 6(e,f)].

Discussion

In this study, local tension transmitted via intercellular junctions was applied to ECs to induce morphological changes in a neighboring EC. The result showed that ECs elongate and orient parallel to the direction of stretch

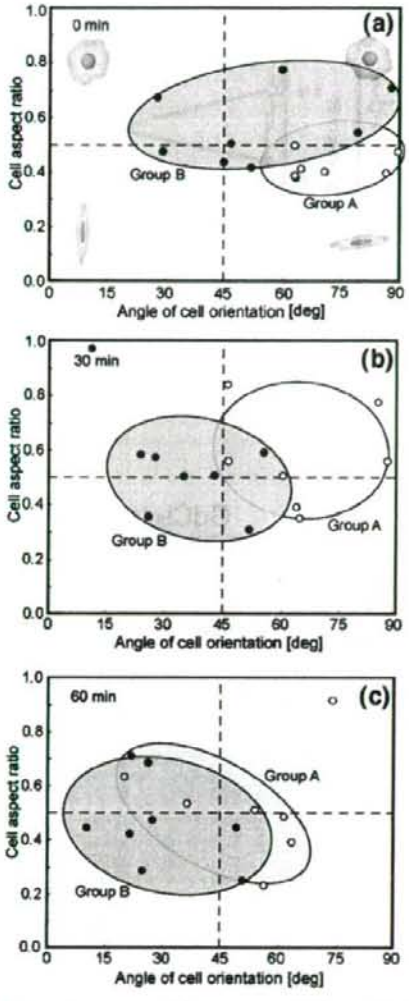

Fig. 4 Changes in morphological parameters of ECs at (**a**) 0 min, (**b**) 30 min and (**c**) 60 min after application of local stretch. Group A represents cells with angle of cell orientation >60° and aspect ratio <0.5 and Group B, the rest of Group A. The two groups showed different time course of changes in the morphological parameters

together with reorganization of stress fibers. Moreover, localization of SHP-2 was selectively observed at intercellular junctions, indicating that mechanotransduction might occur. Most previous studies relating to cell remodeling have utilized global mechanical stimuli including fluid shear stress [1–4] and cyclic stretch [5, 6]. With these conventional techniques, it is difficult to find both mechanotransmission pathways and mechanotransduction sites, probably because these events may occur by a combination of several candidate sensors. To overcome this difficulty, this study proposed a new experimental method to locally apply mechanical stimuli to ECs to identify the role of intercellular junctions involved in EC remodeling.

Interestingly, ECs finally aligned to the direction of stretch at 60 min after application of mechanical stimuli. The mechanism in the present EC remodeling process is unclear. It is well known that ECs exposed to cyclic stretch show alignment perpendicular to the direction of stretch [5]. Sokabe et al. [16] have suggested that when cells are subjected to cyclic stretch, actin cytoskeletons are disassembled during relaxation phase and disruption of actin fibers activates several downstream signals, leading to a cell shape change. On the other hand, ECs under continuous stretch have been shown to align parallel to the direction of stretch [17]. This is consistent with our results in which ECs align to the direction of local continuous stretch, strongly suggesting a critical role of relaxation phase in the EC alignment in response to the two different types of stretch. It is interesting to note that flow-imposed ECs are well known to show alignment to the direction of flow [1, 2, 4]. Although the types of mechanical loadings are different, this tendency is similar to the result of this study in terms of the directional alignment. Several numerical studies have well explained these phenomena of ECs in from the viewpoint of structural optimization. For example, Ohashi et al. [18] reported that ECs exposed to fluid shear stress change their morphology to reduce intracellular stress concentrations. Relating to biomolecular events, Tzima et al. [19] reported that, in ECs exposed to fluid shear stress, Rac1, which is small GTPase controls lamellipodia formation, is locally activated in the downstream region. Likewise, it is worth doing these numerical and extra experimental approaches to elucidate underlying mechanism in the present EC remodeling process. Further investigations may, therefore, include more detailed quantification of intracellular strain field and observations of local activity of Rho small GTPases including Rac1 responsible for reorganization for actin-cytoskeletons.

Time course of change in EC morphology was investigated to characterize EC remodeling process. The remodeling process depended on initial shapes of ECs and thus divided into the two groups: Group A and B. For Group A, ECs initially elongated perpendicular to the direction of stretch exhibited spontaneous contraction prior to elongation/alignment to the direction of stretch. In contrast, for Group B, ECs initially aligned to the direction of stretch immediately exhibited elongation parallel to the direction of stretch. It has been reported that ECs exposed to shear stress show the following time course of change: 1) contraction, 2) reorientation and 3) elongation [7]. Taken

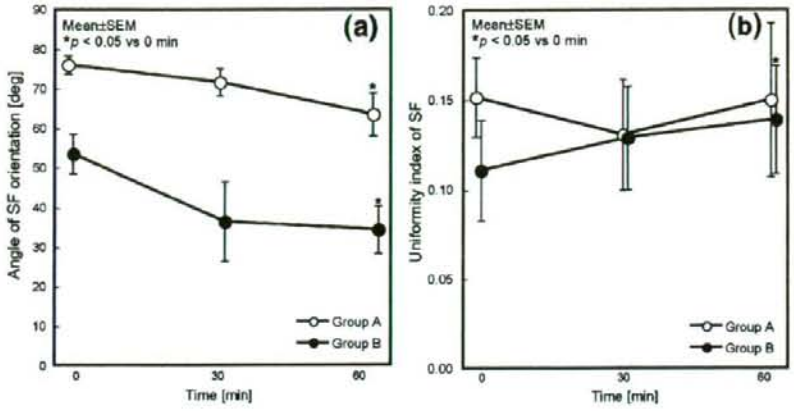

Fig. 5 Time course of changes in SF parameters. (**a**) Angle of SF orientation significantly decreased for both groups. (**b**) Change in uniformity index of SF was not significant for Group A, while the index significantly increased for Group B. See Appendix for details for determination of SF parameters. *$p<0.05$ vs 0 min

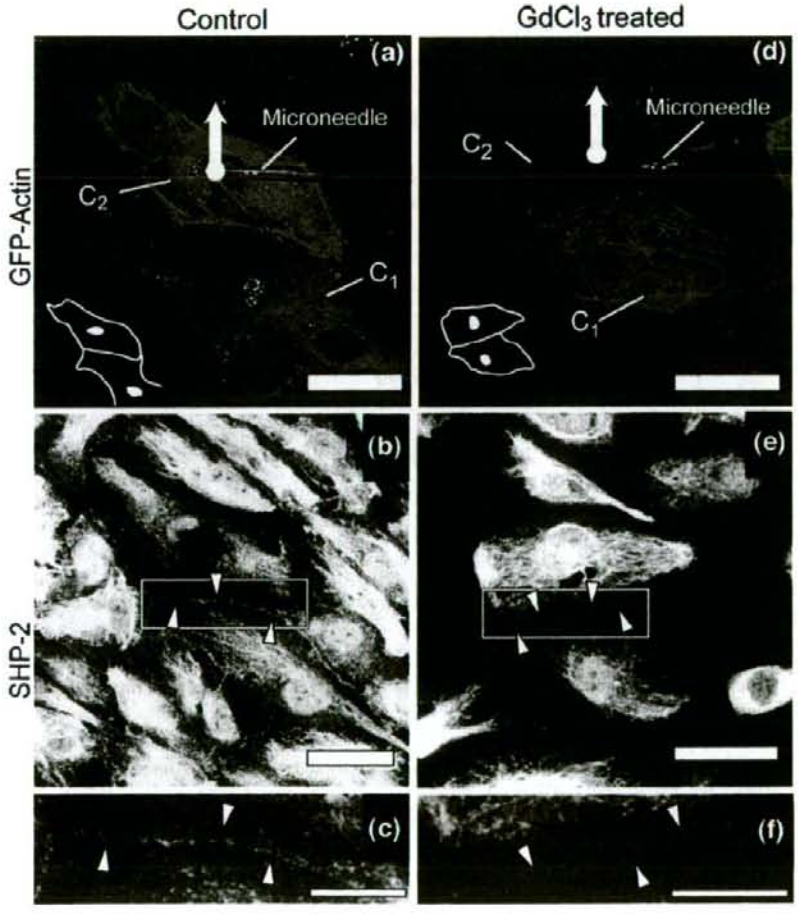

Fig. 6 Typical examples of fluorescent images of SHP-2 for control (**a**, **b**, **c**) and $GdCl_3$ treated ECs (**d**, **e**, **f**). Boxed regions in (**b**) and (**e**) are magnified in (**c**) and (**f**), respectively. Expression of SHP-2 was found to be localized at intercellular junctions (**b**, **d**; arrowheads). Bar=40 μm for (**a**, **b**, **d**, **e**), 20 μm for (**c**, **f**), respectively

these results and our results into consideration, there may exist specific time course of change depending on the type of externally applied mechanical stimuli. It is beyond our findings to see if the present remodeling process might be involved in the EC remodeling exposed to global mechanical stimuli including fluid shear stress. Figure 7 summarizes representative time course of EC remodeling process with GFP-actin together with schematic drawings representing cell morphology and actin organization. This result suggests that cell contraction or low angle of cell orientation should be prerequisite for EC elongation parallel to the direction of stretch. Noria et al. [20] suggested that flow-induced morphological changes of ECs were caused by reorganization of SFs. Moreover, Li et al. [21] reported that ECs transfected with dominant negative RhoA, responsible for SF formation, do not respond to fluid shear

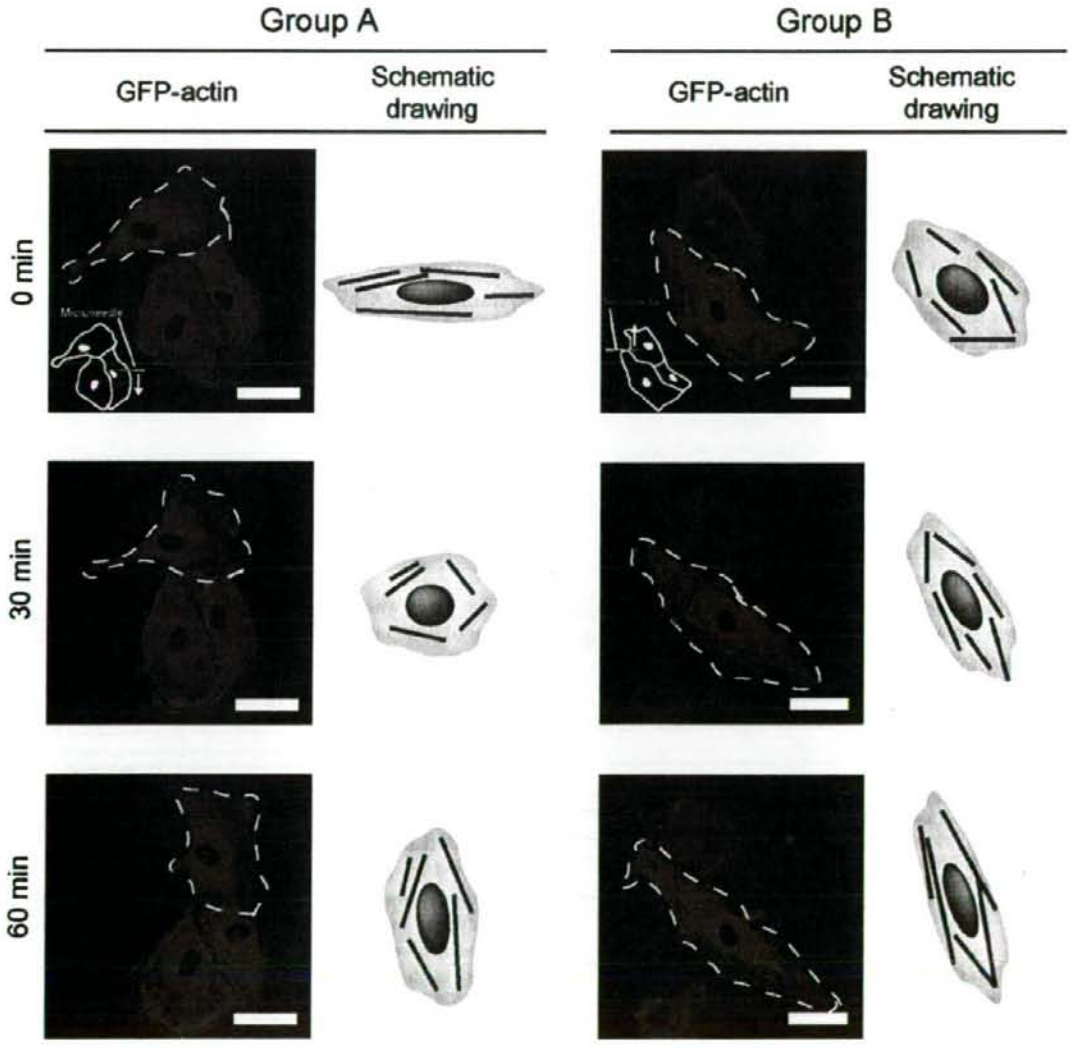

Fig. 7 Representative time course of EC remodeling process with fluorescent images and schematic drawings. Although time courses of change for the two groups are different, the observed ECs (C_1) finally elongated and orientated parallel to the direction of stretch

stress. Taken together, SF reorganization associated with cell morphological changes may play an important role in EC remodeling process.

Well-known mechanotransducers in EC remodeling to mechanical stimuli are SACs, integrins and PECAM-1. SACs are known to be activated by tension. Naruse et al. [22] reported that EC remodeling under exposure to cyclic stretch is inhibited by the blockade of SACs with $GdCl_3$ treatment. In this study, $GdCl_3$ treatment did not significantly affect either morphological changes or localization of SHP-2 at intercellular junctions, indicating that mechanotransduction of SACs does not have a pivotal role in the present EC remodeling. Osawa et al. [13] showed that when mechanotransduction by PECAM-1 occurred, SHP-2 molecules bound to phosphorylated PECAM-1 and recruited to cell-cell borders. Therefore, at least, mechanotransduction by PECAM-1 might be activated by application of local stretch in this study. A recent study [14] suggested that mechanotransduction by PECAM-1 may trigger flow-induced morphological changes of ECs. It is speculated that spatial gradient of magnitude of mechanical stimuli in cells might induce localized mechanotransduction by PECAM-1, possibly leading to the directional EC remodeling. To study this mechanism, further investigations in terms of the quantitative relationship between intracellular stress transfer and SHP-2/PECAM-1 expression should be included.

Conclusions

In this study, local stretch was applied to an EC to stimulate a neighboring EC via intercellular junctions using micromanipulation technique. ECs reorientated and elongated parallel to the direction of stretch. This remodeling process varied from cell to cell, particularly depending on initial cell shape. In addition, SHP-2 was found to be recruited to the stimulated intercellular junctions. These results strongly suggest that intercellular junctions can transmit mechanical forces between cells and transduce the forces into biochemical signals.

Acknowledgement The authors thank Dr. Ikuo Takahashi for kindly providing human umbilical cords. This work was in part supported financially by Grants-in-Aid for Scientific Research from the Ministry of Education, Culture, Sports, Science and Technology (MEXT) in Japan (Nos. 15086203, 17200030, 17680036).

Appendix. Calculation of SF parameters with image processing

The protocol for image processing to determine SF parameters is shown in Fig. 8. Algorithm based on pixel intensity of fluorescence images of GFP-actin was adapted from previous reports [23, 24]. SFs were extracted from original image [Fig. 8(a)] with convolution filter application, as shown in Fig. 8(b). For giving pixels $p_{i,j}$ in 8-bit gray-scale, the pixels surrounding $p_{i,j}$ were selected as a sample matrix [equation (1)]

$$\text{Sample matrix}(S_{i,j}) = \begin{pmatrix} p_{i-2,j-2} & p_{i-2,j-1} & p_{i-2,j} & p_{i-2,j+1} & p_{i-2,j+2} \\ p_{i-1,j-2} & p_{i-1,j-1} & p_{i-1,j} & p_{i-1,j+1} & p_{i-1,j+2} \\ p_{i,j-2} & p_{i,j-1} & p_{i,j} & p_{i,j-1} & p_{i,j+2} \\ p_{i+1,j-2} & p_{i+1,j-1} & p_{i+1,j} & p_{i+1,j+1} & p_{i+1,j+2} \\ p_{i+2,j-2} & p_{i+2,j-1} & p_{i+2,j} & p_{i+2,j+1} & p_{i+2,j+2} \end{pmatrix} \quad (1)$$

Convolution using horizontal and vertical kernels [equations (2) and (3)], which define weighted sum of neighboring pixels, provided magnitude of brightness gradient of SFs in each pixel [equation (4)].

$$\text{Vertical kernel } (K_v) = \begin{pmatrix} -1 & 0 & 2 & 0 & -1 \\ -2 & 0 & 4 & 0 & -2 \\ -4 & 0 & 8 & 0 & -4 \\ -2 & 0 & 4 & 0 & -2 \\ -1 & 0 & 2 & 0 & -1 \end{pmatrix} \quad (2)$$

$$\text{Horizonal kernel } (K_h) = K_v^T \quad (3)$$

$$G = S_{i,j} * K_h + S_{i,j} * K_v \quad (4)$$

The pixel whose G value was bigger than 5-fold of averaged pixel intensity in whole area of the target cell was assigned as a constituent of SFs. In order to calculate the angle of SF orientation, the angle of minimal gradient in pixel intensity in each pixel [Fig. 8(c)] was calculated using Sobel kernels as previously reported [20]. The angle data allocated to only pixels which have been assigned as a constituent of SFs [Fig. 8(d)]. Angle values were summed up across the cell with vectorial summation and were assumed that each pixel has a vector consisted of the calculated angle and unit length. The angle between the direction of the resultant vector and the tensile direction was defined as the angle of SF orientation. The length of the resultant vector divided by the number of pixels was defined as the uniformity index of SFs, which indicate the degree of alignment of SFs. All calculation processes were executed on Excel 2004 for Mac (Microsoft, USA). Analyses were performed on images obtained at every 5 min after application of local stretch.

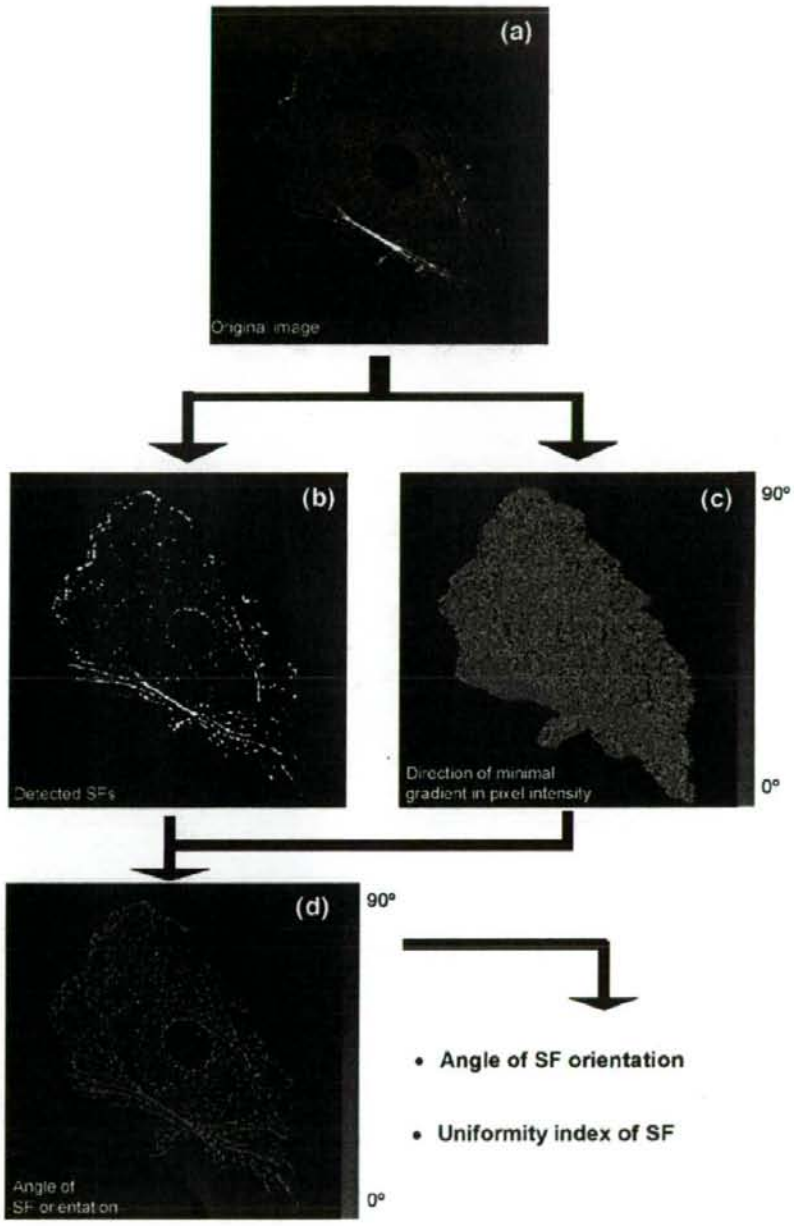

Fig. 8 Protocol for determination of SF parameters based on image processing. (**a**) Manually extracted single cell image, (**b**) automatically detected SFs with convolution filters, (**c**) calculated minimal gradient in pixel intensity with Sobel filter, (**d**) angle of SF orientation in each pixel

References

1. Dewey CF, Bussplari SR, Gimbrone MA, Davies PF (1981) The dynamic response of vascular endothelial cells to fluid shear stress. J Biomech Eng 103:177–185.
2. Galbraith CG, Skalak R, Chien S (1998) Shear stress induces spatial reorganization of the endothelial cell cytoskeleton. Cell Motil Cytoskelet 40:317–330.
3. Sato M, Nagayama K, Kataoka N, Sasaki M, Hane K (2000) Local mechanical properties measured by atomic force microscopy for cultured bovine endothelial cells exposed to shear stress. J Biomech 33:127–135.
4. Kataoka N, Ujita S, Sato M (1998) The effect of flow direction on the morphological responses of cultured bovine aortic endothelial cells. Med Biol Eng Comput 36:122–128.
5. Shirinsky VP, Antonov AS, Birukov KG, Sobolevsky AV, Romanov YA, Kabaeva NV, Antonova GN, Smirnov VN (1989) Mechano-chemical control of human endothelium orientation and size. J Cell Biol 109:331–339.
6. Wang JH, Goldschmidt-Clermont P, Wille J, Yin FC (2001) Specificity of endothelial cell reorientation in response to cyclic mechanical stretching. J Biomech 34:1563–1572.
7. Sugaya Y, Sakamoto N, Ohashi T, Sato M (2003) Elongation and random orientation of bovine endothelial cells in response to hydrostatic pressure: comparison with response to shear stress. JSME Int J Ser C 46:1248–1255.
8. Ohashi T, Sugaya Y, Sakamoto N, Sato M (2007) Hydrostatic pressure influences morphology and expression of VE-cadherin of vascular endothelial cells. J Biomech 40:2399–2405.
9. Albelda SM, Muller WA, Buck CA, Newman PJ (1991) Molecular and cellular properties of PECAM-1 (endoCAM/CD31): a novel vascular cell-cell adhesion molecule. J Cell Biol 114:1059–1068.
10. Ilan N, Cheung L, Pinter E, Madri JA (2000) Platelet-endothelial cell adhesion molecule-1 (CD31), a scaffolding molecule for selected catenin family members whose binding is mediated by different tyrosine and serine/threonine phosphorylation. J Biol Chem 275:21435–21443.
11. Kataoka N, Ujita S, Kimura K, Sato M (1998) The morphological responses of cultured bovine aortic endothelial cells to fluid-imposed shear stress sparse and colony conditions. JSME Int J Ser C 41:76–82.
12. Masuda M, Fujiwara K (1993) Morphological responses of single endothelial cells exposed to physiological levels of fluid shear stress. Front Med Biol Eng 5:79–87.
13. Osawa M, Masuda M, Kusano K, Fujiwara K (2002) Evidence for a role of platelet endothelial cell adhesion molecule-1 in endothelial cell mechanosignal transduction: is it a mechanoresponsive molecule? J Cell Biol 158:773–785.
14. Tzima E, Irani-Tehrani M, Kiosses WB, Dejana E, Schultz DA, Engelhardt B, Cao G, DeLisser H, Schwartz MA (2005) A mechanosensary complex that mediates the endothelial cell response to fluid shear stress. Nature 437:426–431.
15. Sakamoto N, Ohashi T, Sato M (2001) Effect of magnetic field on nitric oxide synthesis of cultured endothelial cells. Int J Appl Electromagn Mech 14:317–322.
16. Sokabe M, Hayakawa K, Tatsumi H (2005) Varieties of mechanotransduction: the cytoskeletal stress fibre as a force transmitter and a mechanosensor. Proc Aust Physiol Soc 36:95.
17. Sasamoto A, Nagino M, Kobayashi S, Naruse K, Nimura Y, Sokabe M (2005) Mechanotransduction by integrin is essential for IL-6 secretion from endothelial cells in response to uniaxial continuous stretch. Am J Physiol, Cell Physiol 288:C1012–1022.
18. Ohashi T, Sugawara H, Matsumoto T, Sato M (2000) Surface topography measurement and intracellular stress analysis of cultured endothelial cells exposed to fluid shear stress. JSME Int J Ser C 43:780–786.
19. Tzima E, Del Pozo MA, Kiosses WB, Mohamed SA, Li S, Chien S, Schwartz MA (2002) Activation of Rac1 by shear stress in endothelial cells mediates both cytoskeletal reorganization and effects on gene expression. EMBO J 21:6791–6800.
20. Noria S, Xu F, McCue S, Jones M, Gotlieb AI, Langille BL (2004) Assembly and reorientation of stress fibers drives morphological changes to endothelial cells exposed to shear stress. Am J Pathol 164:1211–1223.
21. Li S, Chen BP, Azuma N, Hu YL, Wu SZ, Sumpio BE, Shyy JY, Chien S (1999) Distinct roles for the small GTPases Cdc42 and Rho in endothelial responses to shear stress. J Clin Invest 103:1141–1150.
22. Naruse K, Yamada T, Sokabe M (1998) Involvement of SA channels in orienting response of cultured endothelial cells to cyclic stretch. Am J Physiol 274:H1532–1538.
23. Yoshigi M, Clark EB, Yost HJ (2003) Quantification of stretch-induced cytoskeletal remodeling in vascular endothelial cells by image processing. Cytometry A 55:109–118.
24. Kaunas R, Nguyen P, Usami S, Chien S (2005) Cooperative effects of Rho and mechanical stretch on stress fiber organization. Proc Natl Acad Sci 102:15895–15900.

Biorheology 00 (2009) 1–13
DOI 10.3233/BIR-2009-0528
IOS Press

Review

Biomechanical properties of actin stress fibers of non-motile cells *

Shinji Deguchi [a,b] and Masaaki Sato [a,b,**]
[a] *Graduate School of Biomedical Engineering, Tohoku University, Sendai, Japan*
[b] *Graduate School of Engineering, Tohoku University, Sendai, Japan*

Received 21 November 2008
Accepted in revised form 11 February 2009

Abstract. The structure of stress fibers, contractile actin bundles, differs between motile and non-motile cells, though the same term "stress fiber" is used to refer to the structurally as well as functionally different actin bundles. Stress fibers in non-motile cells run between separate focal adhesions, producing isometric tension due to actomyosin contraction. The stress fiber contraction is maintained through dynamic molecular exchanges between preformed and cytoplasmic components. This isometric contraction has been recognized as being essential for extracellular matrix assembly and resultant wound healing. In addition, there have recently been increasing data suggesting that stress fibers under contraction by themselves work as a mechanosensitive element. In this review we discuss, from molecular and physical viewpoints, biomechanical properties of the stress fiber of non-motile cells such as contraction force, resistance to stretching, and their roles in keeping a mechanical homeostasis, which play vital roles in the mechanosensing process.

Keywords: Stress fiber, isometric contraction, mechanical properties, mechanotransduction, actin filament, myosin, α-actinin

1. Introduction

Stress fibers are contractile actin bundles [34]. The bundles are cross-linked by α-actinin, and their contractility is realized by the interaction between actin and double-headed myosin II motor protein with tropomyosin. Such actin bundles containing those proteins appear in both motile cells and non-motile cells [7] and are referred to as a stress fiber in distinction to other actin-based cytoskeletal structures, the lamellipodial actin network or filopodial actin bundles [45]. There have, however, been increasing reports suggesting that structures and functions of stress fibers are different in motile cells and non-motile cells.

Stress fibers in non-motile cells such as vascular endothelial cells elongate and orient in a specific direction in response to fluid shear stress [62] or substrate stretching [31]. The dynamic changes in stress

*This article is based on a plenary lecture given by Dr. Sato at the 13th International Congress of Biorheology and 6th International Conference on Clinical Hemorheology, Pennsylvania State University, PA, USA, July 9–14, 2008.

**Address for correspondence: Dr. M. Sato, Graduate School of Biomedical Engineering, Tohoku University, Sendai 980-8579, Japan. Tel.: +81 22 795 5017; Fax: +81 22 795 5018; E-mail: sato-m@bme.tohoku.ac.jp.